# Investigating lithium-ion battery materials during overcharge-induced thermal runaway: an operando and multi-scale X-ray CT study

Donal P. Finegan, Mario Scheel, James B. Robinson, Bernhard Tjaden, Marco Di Michiel, Gareth Hinds, Dan J. L. Brett, Paul R. Shearing

PCCP

PAPER

View Article Online
View Journal | View Issue



Cite this: *Phys. Chem. Chem. Phys.*, 2016, **18**, 30912

# Investigating lithium-ion battery materials during overcharge-induced thermal runaway: an *operando* and multi-scale X-ray CT study†

Donal P. Finegan,[a] Mario Scheel,[bc] James B. Robinson,[a] Bernhard Tjaden,[a] Marco Di Michiel,[b] Gareth Hinds,[d] Dan J. L. Brett[a] and Paul R. Shearing*[a]

Received 17th June 2016,
Accepted 20th June 2016

DOI: 10.1039/c6cp04251a

www.rsc.org/pccp

Catastrophic failure of lithium-ion batteries occurs across multiple length scales and over very short time periods. A combination of high-speed *operando* tomography, thermal imaging and electrochemical measurements is used to probe the degradation mechanisms leading up to overcharge-induced thermal runaway of a $LiCoO_2$ pouch cell, through its interrelated dynamic structural, thermal and electrical responses. Failure mechanisms across multiple length scales are explored using a post-mortem multi-scale tomography approach, revealing significant morphological and phase changes in the $LiCoO_2$ electrode microstructure and location dependent degradation. This combined *operando* and multi-scale X-ray computed tomography (CT) technique is demonstrated as a comprehensive approach to understanding battery degradation and failure.

## Introduction

Lithium-ion batteries are ubiquitous energy storage devices in portable electronics owing to their high energy and power densities. The synergy between lithium-ion batteries and clean, renewable energy sources to achieve global $CO_2$ emission targets also makes them the technology of choice in the rapidly expanding market for electric and hybrid electric vehicles. However, for many advanced applications, lithium-ion batteries are required to operate safely over a range of temperatures and during high charge and discharge rates. Although failure is rare the consequences are severe and several well publicised incidents[1–3] involving catastrophic battery failures have highlighted the need to further reduce the risk associated with battery packs and modules.[4,5]

Overcharge of lithium-ion batteries poses a significant safety risk as chemical and electrochemical reactions can occur between cell materials, and is one of the primary causes of thermal runaway, as seen in the recent spate of failures associated with charging self-balancing scooters; consequently, overcharge tests have been integrated into safety test standards for lithium-ion batteries.[6,7] The magnitude of the energy released during failure increases with increasing state-of-charge (SOC), as the chemical energy stored in the electrode materials is released, hence thermal runaway resulting from overcharge is particularly catastrophic.[8]

At a critical temperature, thermal runaway takes place when a chain of exothermic reactions between the electrodes and electrolyte occurs. For example, the $LiCoO_2$ positive electrode undergoes exothermic decomposition at elevated temperatures through a series of reduction steps in the presence of electrolyte.[9,10] There have been numerous studies focusing on the reaction pathways of positive electrode materials during failure,[10–13] but a spatial and temporal understanding of the reaction processes and their effects on particle microstructure, rate of reaction and critical temperatures reached during failure, is yet to be achieved.

It is well known that the microstructure of electrode materials plays an important role in determining the performance of cells,[14,15] but the role of particle morphology in the safety of cells is not yet well understood. Jiang and Dahn[16] used accelerated rate calorimetry to investigate the effect of particle size on the onset temperature of thermal runaway, demonstrating that a larger particle size is more thermally stable. More recently, Geder *et al.*[17] demonstrated through thermogravimetric analyses that the mass loss associated with the decomposition of $LiCoO_2$ increases linearly with surface area at 400 °C. A higher mass loss corresponds to increased heat generation during failure, and increased gas (including $O_2$) evolution, further fuelling

[a] *Electrochemical Innovation Lab, Department of Chemical Engineering, University College London, Torrington Place, London WC1E 7JE, UK. E-mail: p.shearing@ucl.ac.uk*
[b] *ESRF, The European Synchrotron, 71 Rue des Martyrs, 38000 Grenoble, France*
[c] *Synchrotron Soleil, L'Orme des Merisiers, 91190 Saint-Aubin, France*
[d] *National Physical Laboratory, Hampton Road, Teddington, Middlesex TW11 0LW, UK*

† Electronic supplementary information (ESI) available. See DOI: 10.1039/c6cp04251a

decomposition of the electrolyte;[18] smaller particles were shown to release more oxygen and have an oxygen deficiency at their surface.

The fast reaction kinetics between the electrolyte and the positive electrode lead to generation of heat at a very high rate, which can result in internal temperatures of commercial cells reaching in excess of 1000 °C,[19] damaging and by-passing integrated safety devices,[20,21] and posing a great risk to modular systems where cell-to-cell propagation of failure is a major concern.[22] Thus, the reliability and safety of lithium-ion batteries is considered a function of the entirety of the cell or modular system. Understanding the link between behaviour on the microscale and the catastrophic effects observed for full cells and modular systems is imperative to progress towards safer battery designs. With the advancement of *operando* X-ray imaging techniques, tracking the propagation of failure at high frame rates and across multiple length scales is now possible.[19,23–25] X-ray computed tomography (CT) has previously been used to perform multi-length scale analyses of battery materials,[26] and has also been demonstrated as an effective diagnostic tool for lithium-ion batteries during,[19,24] and after[27] failure.

Here, we combine high-speed *operando* synchrotron X-ray CT with thermal and electrochemical measurements to link, and assess, the observed morphological, thermal and electrical response of a commercial $LiCoO_2$ battery during overcharge-induced failure. A multi-scale comparative analysis of the cell in its fresh and failed state is also performed to elucidate failure mechanisms across multiple length scales, from individual electrode particles to the full cell architecture. Image-based quantification is used to determine the change in electrode particle morphology *via* a particle size distribution analysis, and the effects of particle morphology on the failure mechanisms of lithium-ion batteries are discussed.

## Experimental

### Electrical abuse testing and *operando* synchrotron CT

Fast tomographic imaging was performed at beamline ID15A at The European Synchrotron (ESRF).[28,29] An *in situ* containment system was designed to allow simultaneous high speed X-ray CT and thermal imaging (Fig. 1a) and is discussed in more detail in a previous work.[19] The overcharge abuse test was performed on a Turnigy nanotech 160 mA h lithium-ion pouch cell (dimensions 39 mm × 12 × 8 mm) which consists of a $LiCoO_2$ positive electrode, polymer separator and graphite negative electrode. The Turnigy cell is designed to cater for high charge (10C) and discharge (30C) rates (where a C-rate is the rate at which a battery is discharged relative to its maximum capacity). In this study the battery was overcharged from 100% SOC (4.2 V) at a constant current of 3 A (18.75 C) until failure, which is well outside the safe operating limits recommended by manufacturers.

Use of an electrical slip ring (P4 + Compact Slip Ring, Moog, UK) built into the ID15A rotation stage (ABR1000, Aerotech, USA)

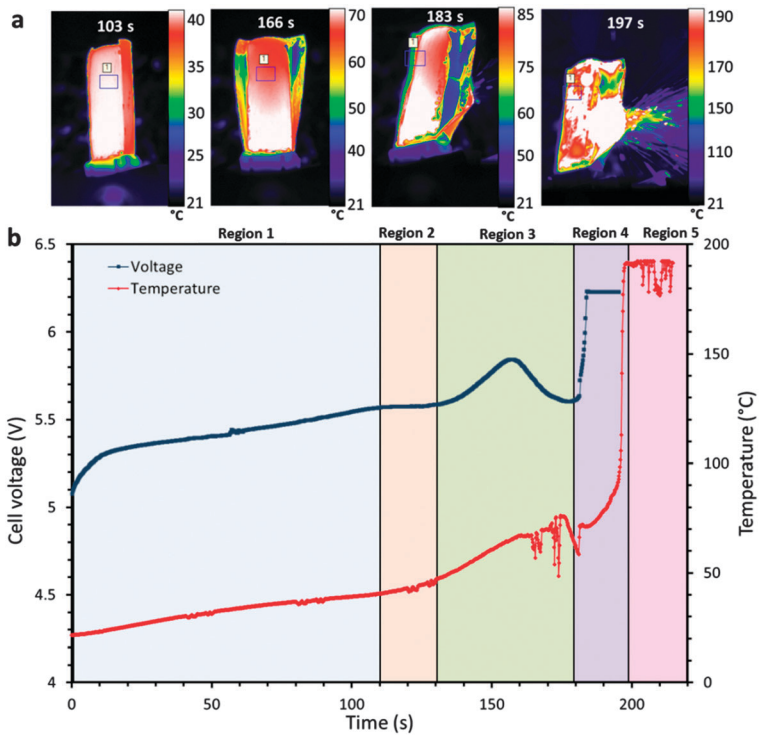


Fig. 1 (a) Sequence of time-stamped thermal images showing the increasing surface temperature of the $LiCoO_2$ pouch cell leading up to thermal runaway. The average temperature within the labelled square is plotted. (b) Plot of the cell voltage and surface temperature, leading up to and during thermal runaway. The battery was charged at a constant current of 3 A (18.75 C), from 100% SOC (4.2 V) until failure. Real time thermal images are presented in Movie S1 (ESI†).

allowed simultaneous rotation of the sample (for X-ray CT) and electrical charging.[19] The cell voltage plot during overcharge is shown alongside the surface temperature profile in Fig. 1b; the temperature presented in the plot was taken as an average over an area *ca.* 9 $mm^2$ on the surface of the cell (shown in Fig. 1a).

The surface temperature of the battery was recorded using a thermal camera (FLIR SC5000MB, FLIR Systems, France). The thermal camera was set to the calibrated range of 15 °C to 200 °C during these experiments. A uniform layer of high emissivity black paint (with a calibrated emissivity of 0.96 over the range 40–180 °C) was applied to the surface of the battery before imaging. The FLIR SC5000MB thermal camera has an extended wavelength detector to capture infra-red wavelengths between 2.5 μm and 7 μm. In the calibrated range, the camera has a noise equivalent temperature difference $<20$ mK. The manufacturer specifies a measurement accuracy of $\pm1$ °C or $\pm1\%$ of the temperature in degrees Celsius. Images were recorded at 25 Hz and the real time movie is provided as Movie S1 (ESI†).

The Turnigy cell was imaged using a 76 keV monochromatic synchrotron X-ray beam. The X-ray absorption signal was converted into a visible light signal by a LuAG:Ce scintillator screen and then collected by a 1× macro objective. A high-speed PCO Dimax CMOS camera (PCO AG, Germany) was used to record the images. The field of view (FOV) was 10.5 mm × 7.6 mm, which consisted of 960 × 700 pixels (horizontal × vertical) and gave a pixel resolution of 10.9 μm. The sample rotation axis was at the edge of the FOV, such that through a 360° rotation it was possible to double the size of the 3D image in the horizontal direction.[30] The resulting 3D reconstruction was then 1785 × 1785 × 700 pixels (19.2 mm × 19.2 mm × 7.6 mm). Each tomogram consisted of 2 × 2000 half projections using an exposure time of 0.7 ms. The acquisition time for each tomogram was 2.8 s and one tomogram was captured every 40 s.

### Multi-scale laboratory X-ray micro-CT

Using material extracted from the same Turnigy cell imaged in the synchrotron, tomographic reconstructions of varying sample size and resolution were produced using lab-based X-ray CT systems (Zeiss Xradia Versa 520 and Zeiss Xradia Ultra 810, Carl Zeiss XRM, Pleasanton, CA, USA). The specific imaging properties for each scan are provided as ESI.† Materials were imaged with a pixel resolution of 63.1 nm (Zeiss Xradia Ultra 810), 0.36 μm (Zeiss Xradia Versa 520) and 7.92 μm (Zeiss Xradia Versa 520). The X-ray CT system (Zeiss Xradia Ultra 810) which achieved a resolution of 63.1 nm uses a chromium target with an accelerating voltage of 35 kV and tube current of 25 mA. The characteristic spectrum from the Cr target is quasi-monochromatic around 5.4 keV. The CT system used for the remaining scans (Zeiss Xradia Versa 520) had a characteristic spectrum from a tungsten target; the accelerating voltage and tube current are user defined and determine the peak intensity of the bremsstrahlung and photon flux. The accelerating voltage and tube current were chosen based on the X-ray absorption coefficients of the samples. The transmission images from all scans were reconstructed using a commercial software package (Zeiss XMReconstructor), which uses an algorithm based on standard filtered back-projection.

### Data processing

The reconstructed tomograms were processed using Avizo Fire 9 software (FEI VSG, France). An edge preserving non-local means filter[31] was applied to the images to reduce noise while maintaining phase boundaries for segmentation. Phases were separated based on grey scale values, where the highly attenuating materials are displayed as white and weakly attenuating materials appear as dark grey. Measurements of sample porosity and particle size distribution were performed using Avizo Fire 9's label analysis tool. The temperature data and thermal imaging videos were extracted using FLIR's Altair software.

## Results and discussion

### Voltage, temperature and *operando* tomography

During overcharge of lithium-ion batteries, a sequence of events related to the evolution of voltage, temperature and chemistry of the cell occurs leading up to thermal runaway and failure. In Fig. 1b, distinctive features can be identified in the temperature and voltage curves. For the initial 110 s (Region 1), the external temperature of the cell increases from 20 °C to *ca.* 40 °C. This initial heating is expected to derive primarily from irreversible heat generation mechanisms, such as Ohmic losses, which are most prevalent at high C rates.[32] A plateau in cell voltage is observed after 110 s (Region 2 in Fig. 1b), followed by a significant increase in the rate of temperature rise after 120 s. The simultaneous voltage plateau and temperature rise indicates the initiation and progression of the decomposition/formation of the solid electrolyte interphase (SEI).[33,34] At high temperatures ($>80$ °C), the SEI becomes unstable and self-discharge initiates. Lee *et al.*[35] suggested that the lithium becomes more active within the carbon lattice at temperatures above 80 °C, causing a large reduction in charge transfer resistance. The combination of the accelerated loss of lithium and the instability of the SEI layer results in an increasing rate of the exothermic SEI decomposition/formation reactions and consumption of lithium.

After *ca.* 80 s, corresponding to an external temperature of 40 °C, the pouch of the cell has begun to swell (Fig. 2) as gas is generated from reduction of the electrolyte and decomposition of the SEI.[36–38] After 120 s, severe delamination is observed around the separator regions in the outer layers. Within Region 3 in Fig. 1b, a distinctive peak in cell voltage occurs over the space of *ca.* 40 s, consistent with the behaviour observed by Belov and Yang.[39] In Movie S1 (ESI†), the pouch structure is seen to diverge from its original packaged structure, which corresponds with this voltage peak, as observed in Fig. 1b. It is expected that the rise in voltage is caused by the resistance increase associated with the gas pockets forming between the active layers, and the subsequent fall in voltage by the decrease in resistance when the pouch bursts and the gases are channelled away. The tightly wound active layers channel gases out into the

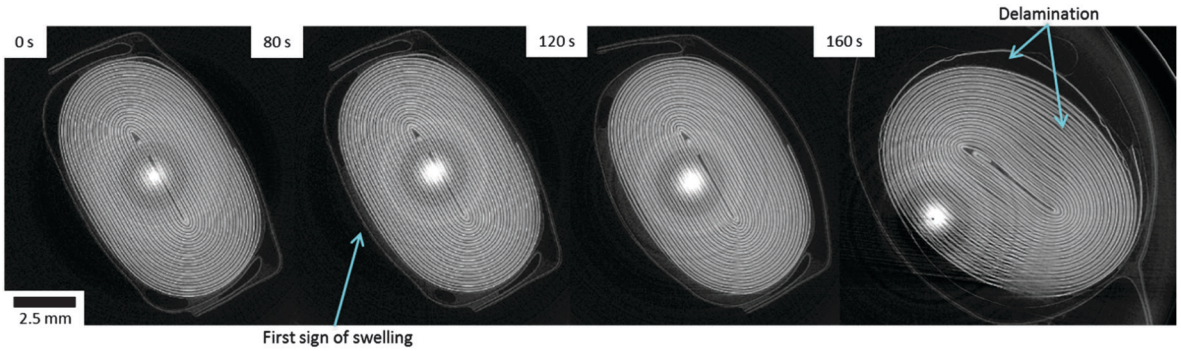


Fig. 2 Time-stamped horizontal slices taken from sequential tomograms during electrical overcharge of the $LiCoO_2$ cell. Pouch swelling begins after 80 s (blue arrow), and the electrode layers begin to deform and delaminate after 160 s. The $LiCoO_2$ electrode also delaminates from the Al current collector after 160 s (blue arrow pointing to inner region).

exterior pouch when the pouch begins to lose its original package structure and starts to swell.

Finally, within Region 4 in Fig. 1b, the cell voltage rises sharply to the maximum voltage of the potentiostat, the most likely cause of which is the shutdown of the separator and damage to the internal circuit caused by the rupture of the cell at that time. The tomogram taken at 160 s in Fig. 2 shows delamination of the $LiCoO_2$ layers from the aluminium current collector in various places, which may be evidence of the electrolyte vaporising or initial stages of decomposition of the $LiCoO_2$ resulting in gas pockets forming between the aluminium current collector and the $LiCoO_2$ layer. This may also be due to the current collector being oxidised by the electrolyte, or the products of electrolyte decomposition.[40,41]

The thermal decomposition of $Li_{0.5}CoO_2$ can occur at temperatures above 200 °C[13] and the reaction between $Li_{0.5}CoO_2$ and solvent (ethylene carbonate), to produce $CO_2$ and $H_2O$, can occur at temperatures as low as 130 °C,[10,13] according to eqn (1).

$$Li_{0.5}CoO_2 + 0.1C_3H_4O_3 \rightarrow 0.5LiCoO_2 + 0.5CoO + 0.3CO_2 + 0.2H_2O \quad (1)$$

Although the surface temperature of the cell appears to be too low for the decomposition of the $LiCoO_2$ to occur, as Lin *et al.* suggested,[42] the cathode side with the aluminium current collector is most susceptible to high temperatures during overcharge abuse. It is also recognised that the temperature measured at the surface of the pouch cell is not deemed representative of the temperature of the internal active materials, due to the thermal insulating effect of the gas between the active materials and the surface of the pouch.

Fluctuations in the surface temperature of the cell occur after around 160 s as the cell ruptures (Movie S1, ESI†), at which point the unstable electrodes are exposed to air and the process of thermal runaway is accelerated. The heat generated from the reaction between the $LiCoO_2$ and electrolyte, along with the decomposition of the SEI layer provide heat for the occurrence of thermal runaway which soon ensues, following which the surface temperature of the cell exceeds the limit of the thermal camera's calibrated range (Region 5 in Fig. 1b).

## Post-mortem CT and battery architecture

For comparison, the full cell was imaged in its fresh state (Fig. 3a) and also post-mortem (Fig. 3b), with a pixel size of 7.92 μm. The structure of the complete cell before and after thermal runaway is compared and the extent of structural damage and material degradation investigated. The aluminium (Al) phase was segmented (blue phase in Fig. 3b), and is shown to have agglomerated at the top and bottom of the wound electrode layers. The rapid gas generation from the decomposition of the $LiCoO_2$ and electrolyte is likely to have carried the molten Al to the ends of the roll as the gas was channeled from the inner layers to the outer pouch. The porous structure of the Al globules at either end of the cell supports the hypothesis that gas played a part in carrying the molten metal. The uneven gas generation may also have had a peristaltic effect between the tightly wound layers, forcing the molten Al to either end.

Fig. 4a–d compares the structure of the $LiCoO_2$ electrode before and after thermal runaway. The pixel sizes for the fresh and post-mortem tomograms in Fig. 4 were 0.424 μm and 0.36 μm respectively. In its fresh state the $LiCoO_2$ is coated uniformly onto the Al current collector (Fig. 4a and b) which is *ca.* 13 μm thick. As seen in Fig. 4c and d, the Al layer between the remains of the

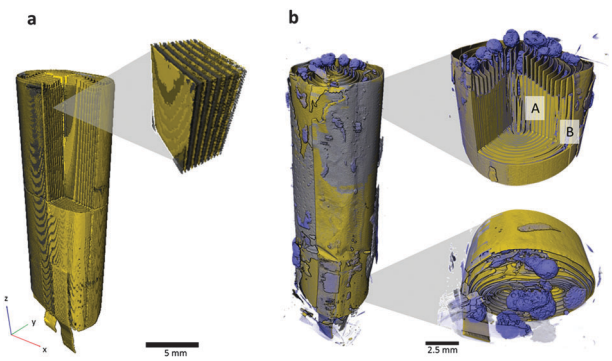


Fig. 3 (a) 3D reconstruction of the pouch cell in its fresh state. The $LiCoO_2$ electrode is displayed as grey, and the copper current collector and tabs are shown in yellow. (b) 3D reconstruction showing the pouch cell after overcharge-induced thermal runaway. Copper and $LiCoO_2$ phases are labelled as yellow and aluminium is shown in blue. Samples were taken from regions A and B for further analysis using micro-X-ray CT.

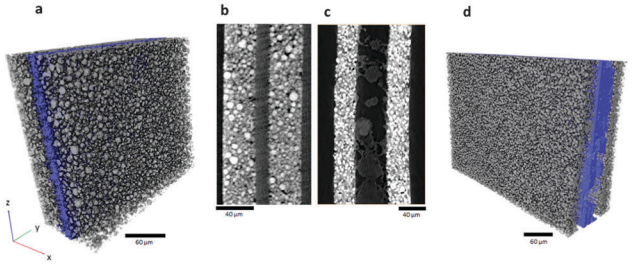


Fig. 4 (a) 3D reconstruction of aluminium current collector (blue) coated with $LiCoO_2$ (grey) in its fresh state alongside an *XZ* orthoslice (b). (c) and (d) show an *XZ* orthoslice and 3D reconstruction of the current collector and the remains of $LiCoO_2$ after thermal runaway.

$LiCoO_2$ is highly porous following thermal runaway and cooling. The $LiCoO_2$ layers are much further apart, now *ca.* 40–50 μm, which would have aided the escape of gases generated during the thermal runaway process. The high specific heat and thermal conductivity of Al would also have enhanced the heat dissipation of local exothermic reactions leading up to and during thermal runaway. The melting point of Al is 660 °C and hence the distribution of molten aluminium remnants in Fig. 3 and 4 demonstrates that the interior of the cell reached in excess of 660 °C. As seen at the bottom of the cell in Fig. 3b, only a small portion of the cell in the region of the current collecting tab appears to have reached the melting point of copper (1085 °C). The temperature range between 660 °C and 1085 °C presents the possibility of further decomposition reactions occurring, evidence of which is found upon further investigation of the individual $LiCoO_2$ particles post-mortem.

### Micro-CT and particle structure degradation

The size and shape of particles have been shown to play a significant role in the thermal stability of electrode materials and influence the magnitude of catastrophic failure upon thermal runaway.[16,17] The decomposition reactions of $LiCoO_2$ to $Co_3O_4$, CoO and further to Co metal occur at elevated temperatures and in the presence of organic electrolyte at the surface of the particles. For example, at >150 °C, the following reduction reactions can occur where solv. indicates the reaction step occurs in the presence of electrolyte solvent.[10]

$$Li_{0.5}CoO_2 \xrightarrow{>150\ ^\circ C} 0.5LiCoO_2 + \frac{1}{6}Co_3O_4 + \frac{1}{6}O_2 \quad (2)$$

$$Co_3O_4 \xrightarrow{>150\ ^\circ C,\ solv.} 3CoO + \frac{1}{2}O_2 \quad (3)$$

$$CoO \xrightarrow{>150\ ^\circ C,\ solv.} Co + \frac{1}{2}O_2 \quad (4)$$

Additionally, $CO_2$ evolved from degradation reactions (1) and combustion reactions of the solvent and separator, could react with any remaining $LiCoO_2$ particles according to (5), resulting in additional formation of Co metal.

$$2LiCoO_2 + CO_2 \xrightarrow{>150\ ^\circ C,\ solv.} Li_2CO_3 + 2Co + \frac{3}{2}O_2 \quad (5)$$

Most of these reactions occur at the interface between the transition metal oxide and electrolyte. Larger particle surface area increases the probability of surface degradation reactions; hence, with reduced particle size the specific surface area exposed to the electrolyte increases and the rate at which exothermic degradation reactions occur would be greater. Post-mortem micro-CT of the $LiCoO_2$ particles shows severe microstructural degradation (Fig. 5). Evidence of a surface layer of Co metal on the electrode particles is seen in Fig. 5a. Fig. 5b shows a greyscale 2D slice with the highly attenuating Co layer (white) at the surface of the particle. A semi-transparent 3D

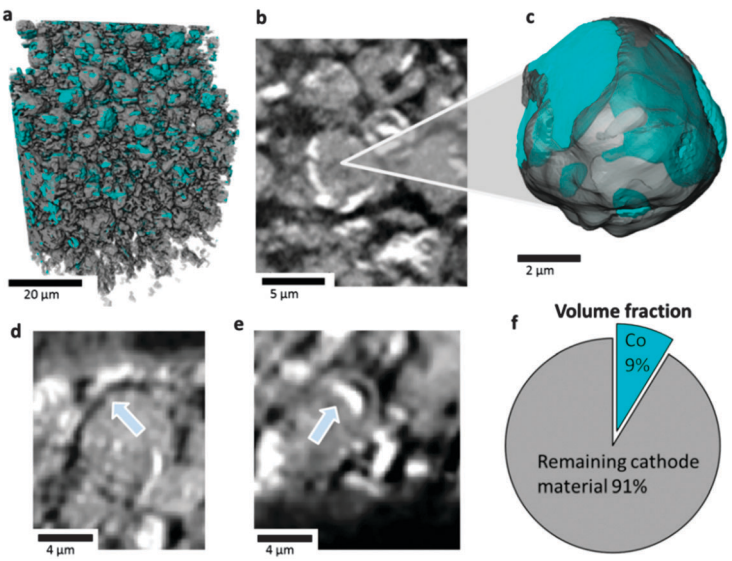


Fig. 5 (a) 3D rendering of a portion of $LiCoO_2$ electrode showing isolated Co phase (teal); (b) greyscale slice view of $LiCoO_2$ particle showing evidence of phase separation based on attenuation and (c) semi-transparent 3D visualisation of $LiCoO_2$ particle (grey) showing surface and sub-surface presence of Co (teal); (d and e) greyscale slice views showing delamination of Co metal surface layer; (f) 2D representation of the volume fraction of Co within the remaining $LiCoO_2$ electrode material. This sample was extracted from an inner region labelled as A in Fig. 3.

 

rendering of the particle (Fig. 5c) shows the presence of Co (teal) on the surface and Co channels within the particle. As a result of changes in density of materials during decomposition, a reduction in particle volume and delamination of phases is expected to occur. The density of Co metal is almost twice that of $LiCoO_2$ and accordingly, there is evidence of delamination of the Co layer from the bulk of the particle, shown in Fig. 5(d and e). During thermal runaway, this delamination would have exposed further surface material to exothermic reduction.

From attenuation coefficients of expected decomposition products (see ESI†) the composition of the particle surface layer and interior can be inferred; the difference in greyscale between the Co surface layer and the particle interior suggests that most of the particle consists of CoO, which is consistent with previous XRD experiments.[10] The volume fraction of Co metal in the remaining cathode material is calculated to be 9% (Fig. 5f). SEM images and EDS (Fig. 6a and b) show that the surface of the particle consists of Co globules rather than the smooth surface presented in Fig. 5; this is due to the limited resolution of the X-ray CT technique to resolve fine surface features.[26] The surface of the $LiCoO_2$ particles after thermal runaway appears relatively rough when compared to the fresh sample presented in Fig. 6c, which is ascribed to shrinkage of the Co-oxide as it is reduced, and delamination and agglomeration of Co metal. Additionally, subsurface Co metal seams are present in the tomograms which could also be explained by the infiltration of electrolyte through micro-cracks and fractures, which could not be resolved in the CT images.

Without excess electrolyte and high temperature ($>350$ °C) it is expected that the air-stable $Co_3O_4$ and CoO would not be reduced to Co.[43] Three samples were taken from subsurface layers (Region A in Fig. 3b), each of which showed the presence of Co on the surface when analysed under CT; however, a sample taken from the surface of the cell (region B in Fig. 3b) did not show any presence of Co on the surface of the particles (Fig. 7). This may have been due to the outer regions having a lower local temperature (due to enhanced heat rejection) and insufficient quantities of electrolyte for the final reduction step to occur. As shown in a previous study,[19] temperature differences of $>700$ °C can occur over as little as 7 mm during thermal runaway, where the outer regions of the cell remain relatively cool and the inner regions can reach $>1000$ °C. Hence, at the outer regions the conditions (temperature and retention of electrolyte) are less favourable to sustaining the propagation of thermal runaway, making the extent of exothermic degradation location dependent.

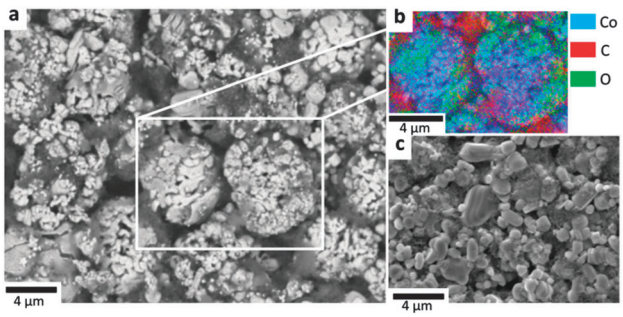


Fig. 6 (a) SEM micrograph of the $LiCoO_2$ material after overcharge and thermal runaway, (b) EDS of the highlighted region showing that the surface layer consists of Co metal, and (c) SEM micrograph of the fresh $LiCoO_2$ particles.

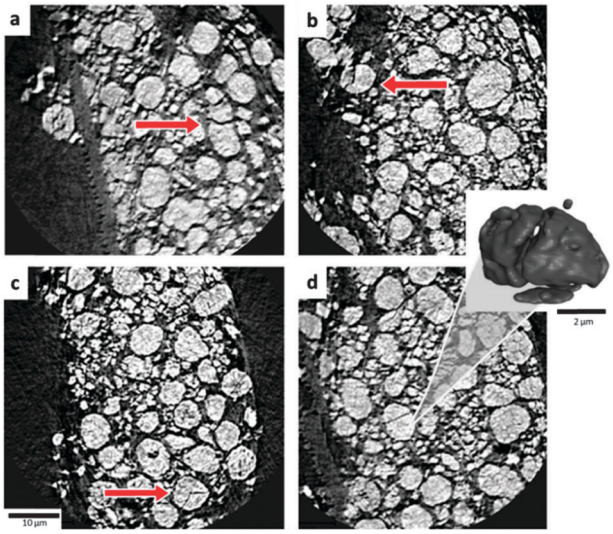


Fig. 7 (a–d) Orthoslices highlighting cracked $LiCoO_2$ particles. Sample was extracted from the outer region labelled as B in Fig. 3. Inset: An isolated 3D volume of the cracked particle in (d).

In contrast to the subsurface samples, the surface sample presented in Fig. 7 contains numerous fractured particles. As Geder *et al.*[17] demonstrated, a reduced particle size (and increased specific surface area) results in unfavourable consequences, such as a higher rate of heat generation and lower onset temperatures for thermal runaway.

### Particle size distribution

Mass loss occurs at each reduction step according to eqn (2)–(4), and the electrode particles are expected to reduce in mass and volume, and increase in density. The particle size distribution (PSD) of a fresh sample is compared with that of both post-mortem samples; the inner sample (showing presence of a Co surface layer) and the outer sample (showing significant cracking and the absence of Co). The particle volumes used for the PSD of the three samples were 24 897 $\mu m^3$ (fresh), 34 907 $\mu m^3$ (inner), and 33 785 $\mu m^3$ (outer). The PSD for each sample is presented in Fig. 8. In its fresh state the PSD centres around a mean diameter 3.87 μm with a relatively low standard deviation. There is a significant decrease in the mean diameter of the remaining particles for both post-mortem samples to approximately half their original size (to 1.99 μm and 1.97 μm for the inner and outer samples respectively), but the spread of data in the PSD greatly differs (Fig. 8). The PSD for the inner sample shows a single peak which has shifted below 2 μm, which is due to a combination of particle shrinkage during phase transitions and the presence of significant debris consisting of fractured particles and delaminated Co. In contrast, a bimodal PSD is

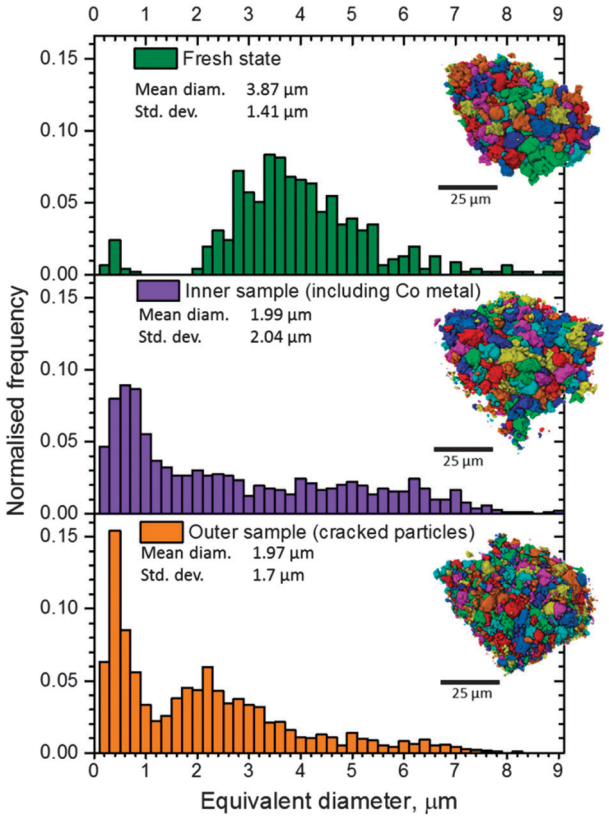


Fig. 8 Particle size distributions for $LiCoO_2$ particles from a fresh sample (top), a sample taken from the inner regions of the failed overcharged cell showing evidence of complete reduction to Co metal (middle), and a sample taken from the outer region of the failed overcharged cell showing evidence of particle cracking with no formation of Co (bottom).

observed for the outer sample (cracked particles). When compared to the PSD of the fresh sample, the twin peaks correspond to the occurrence of particle cracking, where the majority of the distribution is shifted to a smaller equivalent particle diameter. However, a second peak which consists of particles $<1$ μm in diameter contains the highest frequency of particles. This second peak may reflect smaller particle fragments from the fractured larger particles. Due to the limited resolution of the X-ray CT technique, the specific surface area of the particles could not be accurately determined; however, the dramatic reduction in particle size observed between the fresh and outer samples is expected to significantly affect the rate of decomposition of the electrode at elevated temperatures. Additional surface area would be exposed to reaction with the electrolyte and the smaller fragmented particles would exhibit a lower onset temperature.[16,17] For example, as demonstrated by Jiang and Dahn,[16] a reduction in particle size of $LiCoO_2$ from 5 μm to 0.8 μm results in decreased thermal stability, with lower onset temperatures.

Although it is well known that the particle shape and size significantly affect the onset temperature and rate of heat generation during thermal runaway, it is not well understood how the evolving microstructure and likelihood of particle fracture influence these properties leading up to and during the runaway process. Further work is required to quantify the change in particle structure based on the conditions to which the particles are subjected, and the effect of initial particle morphology on the rate and quantity of heat generation during thermal runaway. As X-ray CT techniques continue to achieve higher spatial and temporal resolution, the dependence of morphological evolution on particle size, and its consequent effect on the magnitude of failure, could also be explored *via operando* micro-CT. A large particle size with low surface area may provide a more thermally stable electrode, but can also result in a reduction of the cell's power density; hence a balance between battery performance and safety may exist. Understanding the mechanisms through which particle architecture and properties change during thermal runaway is also essential to progress towards an optimised particle size distribution for both performance and safety.

## Conclusions

This comprehensive approach of combined high speed *operando* X-ray CT and thermal imaging, followed by post-mortem multi-scale X-ray CT and SEM analyses, has provided new insights into the failure mechanisms of lithium-ion batteries. The effects of heating and gas generation on the architecture of the cell have been explored during failure *via* high-speed *operando* tomography, showing electrode layer delamination, gas pocket formation and consequent swelling of the pouch. Multi-scale comparative analyses of the complete cell, as well as separate components of the cell, before and after thermal runaway, have elucidated key phenomena that contribute to the propagation and severity of thermal runaway; the presence of agglomerated aluminium at both ends of the cell demonstrates the effective heat transfer throughout the cell *via* molten Al during failure.

X-ray CT of the electrode particle microstructures in samples taken from different locations within the cell presents valuable information on the local kinetics and progress of exothermic reduction reactions at the positive $LiCoO_2$ electrode. The volume fraction of Co, and its presence on the surface of the electrode particles, indicates that the rate of exothermic reduction steps, and therefore heat generation, is dependent on the surface area and PSD of the positive electrode. The extreme thermal and electrical conditions during overcharge-induced thermal runaway cause the particle morphology, and hence the PSD and specific surface area, to change.

The results of this work show that particle microstructure can significantly influence the extent and rate of exothermic degradation reactions during thermal runaway, and demonstrate that X-ray CT could be used to elucidate the relationship between electrode microstructure and overall safety of commercial cells.

## Acknowledgements

The authors gratefully acknowledge funding from the Engineering and Physical Sciences Research Council (EPSRC), the Royal Academy of Engineering and the National Physical Laboratory (NPL).

We are grateful to the STFC for travel funding through the Global Challenge Network in Batteries and Electrochemical Energy Devices. These experiments were performed on the ID15A beamline at the ESRF, Grenoble, France. The French National Research Agency (ANR) is acknowledged for support *via* EQUIPEX grant ANR-11-EQPX-0031 (project NanoimagesX).



## References

1 NTSB, Aircraft Incident Report, Auxiliary Power Unit Battery Fire, Japan Airlines Boeing 787-8, JA829J, Report PB2014-108867, National Transport Safety Board, 2014.
2 JTSB, Aircraft Serious Incident Investigation Report, All Nippon Airways Co., LTD JA804A, Report AI2014-4, Japan Transport Safety Board, 2014.
3 AAIB, Report on the serious incident to Boeing B787-8, ET-AOP London Heathrow Airport on 12 July 2013, Report Air accident report: 2/2015, 2015.
4 N.-S. Choi, Z. Chen, S. A. Freunberger, X. Ji, Y.-K. Sun, K. Amine, G. Yushin, L. F. Nazar, J. Cho and P. G. Bruce, *Angew. Chem., Int. Ed.*, 2012, **51**, 9994–10024.
5 J. B. Goodenough and Y. Kim, *Chem. Mater.*, 2009, **22**, 587–603.
6 UN Manual of Tests and Criteria, Part III: those relating to assignment of substances or articles to Class 2, Class 3, Class 4, Division 5.1, Class 8 or Class 9, United Nations, New York, 2009, Section 38.3: Lithium Metal and Lithium Ion Batteries.
7 D. H. Doughty and C. Crafts, *FreedomCAR Electrical Energy Storage System Abuse Test Manual for Electric and Hybrid Electric Vehicle Applications*, Sandia National Laboratories, 2006.
8 F. Larsson and B.-E. Mellander, *J. Electrochem. Soc.*, 2014, **161**, A1611–A1617.
9 C.-H. Doh, D.-H. Kim, H.-S. Kim, H.-M. Shin, Y.-D. Jeong, S.-I. Moon, B.-S. Jin, S. W. Eom, H.-S. Kim, K.-W. Kim, D.-H. Oh and A. Veluchamy, *J. Power Sources*, 2008, **175**, 881–885.
10 D. D. MacNeil and J. R. Dahn, *J. Electrochem. Soc.*, 2002, **149**, A912–A919.
11 R. A. Leising, M. J. Palazzo, E. S. Takeuchi and K. J. Takeuchi, *J. Power Sources*, 2001, **97–98**, 681–683.
12 R. A. Leising, M. J. Palazzo, E. S. Takeuchi and K. J. Takeuchi, *J. Electrochem. Soc.*, 2001, **148**, A838–A844.
13 D. D. MacNeil and J. R. Dahn, *J. Electrochem. Soc.*, 2001, **148**, A1205–A1210.
14 D.-W. Chung, P. R. Shearing, N. P. Brandon, S. J. Harris and R. E. García, *J. Electrochem. Soc.*, 2014, **161**, A422–A430.
15 M. Jo, Y.-S. Hong, J. Choo and J. Cho, *J. Electrochem. Soc.*, 2009, **156**, A430–A434.
16 J. Jiang and J. R. Dahn, *Electrochim. Acta*, 2004, **49**, 2661–2666.
17 J. Geder, H. E. Hoster, A. Jossen, J. Garche and D. Y. W. Yu, *J. Power Sources*, 2014, **257**, 286–292.
18 J. R. Dahn, E. W. Fuller, M. Obrovac and U. von Sacken, *Solid State Ionics*, 1994, **69**, 265–270.
19 D. P. Finegan, M. Scheel, J. B. Robinson, B. Tjaden, I. Hunt, T. J. Mason, J. Millichamp, M. Di Michiel, G. J. Offer, G. Hinds, D. J. L. Brett and P. R. Shearing, *Nat. Commun.*, 2015, **6**, 6924.
20 P. G. Balakrishnan, R. Ramesh and T. Prem Kumar, *J. Power Sources*, 2006, **155**, 401–414.
21 Z. Chen, Y. Qin and K. Amine, *Electrochim. Acta*, 2009, **54**, 5605–5613.
22 C. F. Lopez, J. A. Jeevarajan and P. P. Mukherjee, *J. Electrochem. Soc.*, 2015, **162**, A1905–A1915.
23 M. Ebner, F. Marone, M. Stampanoni and V. Wood, *Science*, 2013, **342**, 716–720.
24 D. P. Finegan, E. Tudisco, M. Scheel, J. B. Robinson, O. O. Taiwo, D. S. Eastwood, P. D. Lee, M. Di Michiel, B. Bay, S. A. Hall, G. Hinds, D. J. L. Brett and P. R. Shearing, *Adv. Sci.*, 2016, **3**, 1500332, DOI: 10.1002/advs.201500332.
25 D. S. Eastwood, V. Yufit, J. Gelb, A. Gu, R. S. Bradley, S. J. Harris, D. J. L. Brett, N. P. Brandon, P. D. Lee, P. J. Withers and P. R. Shearing, *Adv. Energy Mater.*, 2014, **4**, 1300506.
26 P. R. Shearing, N. P. Brandon, J. Gelb, R. Bradley, P. J. Withers, A. J. Marquis, S. Cooper and S. J. Harris, *J. Electrochem. Soc.*, 2012, **159**, A1023–A1027.
27 V. Yufit, P. Shearing, R. W. Hamilton, P. D. Lee, M. Wu and N. P. Brandon, *Electrochem. Commun.*, 2011, **13**, 608–610.
28 A. Rack, M. Scheel, L. Hardy, C. Curfs, A. Bonnin and H. Reichert, *J. Synchrotron Radiat.*, 2014, **21**, 815–818.
29 M. Di Michiel, J. M. Merino, D. Fernandez-Carreiras, T. Buslaps, V. Honkimäki, P. Falus, T. Martins and O. Svensson, *Rev. Sci. Instrum.*, 2005, **76**, 043702.
30 A. Kyrieleis, M. Ibison, V. Titarenko and P. J. Withers, *Nucl. Instrum. Methods Phys. Res., Sect. A*, 2009, **607**, 677–684.
31 A. Buades, B. Coll and J. Morel, *Multiscale Model. Simul.*, 2005, **4**, 490–530.
32 C. Heubner, M. Schneider and A. Michaelis, *J. Power Sources*, 2016, **307**, 199–207.
33 Z. Chen, Y. Qin, Y. Ren, W. Lu, C. Orendorff, E. P. Roth and K. Amine, *Energy Environ. Sci.*, 2011, **4**, 4023–4030.
34 H. Yang, H. Bang, K. Amine and J. Prakash, *J. Electrochem. Soc.*, 2005, **152**, A73–A79.
35 H. H. Lee, C. C. Wan and Y. Y. Wang, *J. Electrochem. Soc.*, 2004, **151**, A542–A547.
36 T. Ohsaki, T. Kishi, T. Kuboki, N. Takami, N. Shimura, Y. Sato, M. Sekino and A. Satoh, *J. Power Sources*, 2005, **146**, 97–100.
37 A. W. Golubkov, D. Fuchs, J. Wagner, H. Wiltsche, C. Stangl, G. Fauler, G. Voitic, A. Thaler and V. Hacker, *RSC Adv.*, 2014, **4**, 3633–3642.
38 J.-H. Kim, N. P. W. Pieczonka and L. Yang, *ChemPhysChem*, 2014, **15**, 1940–1954.
39 D. Belov and M.-H. Yang, *ECS Trans.*, 2007, **6**, 29–44.
40 E. Krämer, S. Passerini and M. Winter, *ECS Electrochem. Lett.*, 2012, **1**, C9–C11.
41 D. Belov and M.-H. Yang, *J. Solid State Electrochem.*, 2008, **12**, 885–894.
42 C.-K. Lin, Y. Ren, K. Amine, Y. Qin and Z. Chen, *J. Power Sources*, 2013, **230**, 32–37.
43 Z. Lendzion-Bieluń, R. Jędrzejewski and W. Arabczyk, *Cent. Eur. J. Chem.*, 2011, **9**, 834–839.